Bidirectional zigzag growth from clusters of active colloidal shakers

Gaspard Junot [1], Andrés Javier Manzano González,[1] and Pietro Tierno [1,2,3,*]

[1]*Departament de Física de la Matèria Condensada, Universitat de Barcelona, 08028 Spain*
[2]*Universitat de Barcelona Institute of Complex Systems (UBICS), Universitat de Barcelona, Barcelona, 08028 Spain*
[3]*Institut de Nanociència i Nanotecnologia, Universitat de Barcelona, Barcelona, 08028 Spain*

Driven or self-propelling particles moving in viscoelastic fluids recently emerged as a novel class of active systems showing a complex yet rich set of phenomena due to the non-Newtonian nature of the dispersing medium. Here we investigate the one-dimensional growth of clusters made of active colloidal shakers, which are realized by oscillating magnetic rotors dispersed within a viscoelastic fluid and at different concentrations of the dissolved polymer. These magnetic particles when actuated by an oscillating field display a flow profile similar to that of a shaker force dipole, i.e., without any net propulsion. We design a protocol to assemble clusters of colloidal shakers and induce their controlled expansion into elongated zigzag structures. We observe a power law growth of the mean chain length and use theoretical arguments to explain the measured 1/3 exponent. These arguments agree well with both experiments and particle based numerical simulations.

I. INTRODUCTION

Investigating the formation of dynamic patterns from a collection of active or self-propelling particles is a rich research field that has led to the observation of fascinating phenomena including swarming [1–4], clustering [5–10], crystallization [11,12], dynamic vortices and swirls [13–15], or phase separation induced by motility [16–19], among others. Moreover, collective ensemble of active particles that can be controlled by an external field may be used as "progammable matter" to perform useful tasks at the microscale, with potential applications in robotics [20–22], microfluidics [23,24], or material science [25].

While most of the prototypes realized so far have been dispersed in Newtonian fluids, such as water, many new interesting effects may arise when the fluid medium is non-Newtonian, such as a viscoelastic one [26–32]. Indeed, in biological systems microorganisms such as sperm cells navigate in a non-Newtonian fluid. The nonlinearity of the dispersing medium may affect the sperm transport [33] apart from being important in several other processes including biofilm formation [34,35] or fertilization [36]. As previously reported, a viscoelastic medium may even induce propulsion to a reciprocal swimmer which performs periodic, time-reversible, body-shape deformations [37].

In a recent experimental work [38], we reported the formation of large scale zigzag bands made of a population of magnetic rotors which were reversibly actuated by an external, oscillating magnetic field. When the magnetic rotors oscillate in water, the particles perform periodic back-forward rolling being unable to organize in any significant structure, i.e., they remain evenly distributed across the plane. In contrast, by adding a small amount of polymer that makes the medium viscoelastic, we observe that the particles self-organize into zigzag structures which merge in time perpendicular to the direction of the oscillating field. The progressive coarsening of these bands would ultimately lead to the formation of a single chain of particles with the size of the system. In our previous work [38], it was not possible to investigate the elongation dynamics and reach the steady state since thick bands, as the one shown in Fig. 1(b), extend above the observation area. Moreover, these bands reached the boundaries of the experimental cell, thus interacting with the confining walls.

To study the evolution of the system toward its steady state, we have developed a protocol to create isolated clusters from which smaller bands grow, sufficiently far from neighboring bands and from the confining walls. Under these conditions, we report a growth process that could not be observed in Ref. [38]. Indeed, when isolated, thin bands laterally extend while reducing their thickness over time. We observe a power law growth of these lines and analyze in detail the influence of the polymer concentration on the velocity field generated by a particle as well as on the growth process. Finally, using a simple theoretical argument based on conservation law, we explain the growth and the observed 1/3 exponent. We confirm these predictions by doing particle based numerical simulations that agree both with the model and the experiments.

II. EXPERIMENTAL SYSTEM

Our colloidal shakers are realized by cyclically actuating anisotropic hematite microparticles in a viscoelastic medium. As shown in the top inset of Fig. 1(a), the hematite are characterized by two connected spherical lobes of equal diameters $b = 1.2 \, \mu m$ with a total length of $a = 2.6 \, \mu m$. This peanutlike shape of the particles is the result of their chemical
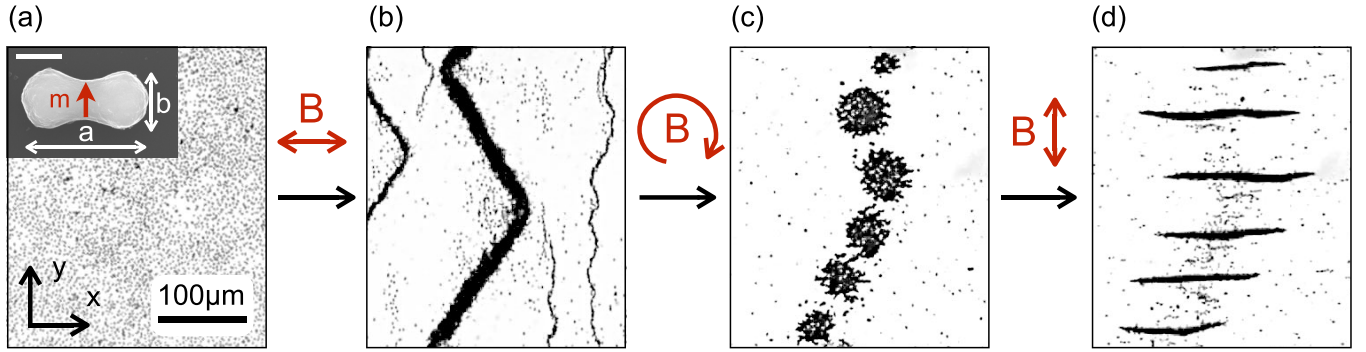
FIG. 1. (a)–(d) Sequence of experimental images showing the protocol employed to generate growing clusters of colloidal shakers. We start from a homogeneous dispersion of particles in a mixture of water and PAAM, as shown in (a). We first apply a rotating field polarized in the $(\hat{x}, \hat{z})$ plane, Eq. (1), which induces the growth of zigzag bands along the perpendicular one (y), as shown in (b). After that, an in-plane $(\hat{x}, \hat{y})$ rotating magnetic field is used to break the band into a sequence of circular clusters (c). Then the applied field is switched such that it rotates in the $(\hat{y}, \hat{z})$ plane, and it induces the grow of parallel zigzag structures, as shown in (d). Details on the field parameters are given in the text, the scale bar for all images is 100 μm. Top inset in (a) shows a scanning electron microscope image of a hematite particle with dimensions ($a = 2.6$ μm, $b = 1.2$ μm) and the direction of the permanent moment m. The scale bar is 1 μm. The sequence of images (c), (d) is shown in video S1 in [39].

synthesis, performed following the sol gel approach [40]; more detail can be found in a previous work [41]. The particles are ferromagnetic and characterized by a permanent moment directed perpendicular to their long axis, with magnitude $m \simeq 9 \cdot 10^{-16}$ Am^2 [42]. We disperse these particles in a viscoelastic medium made of a water solution of polyacrylamide (PAAM), a water soluble high-molecular weight polymer ($M_w = 5 - 6 \cdot 10^6$). In this work we change the polymer concentration within the range $c_p \in [0, 0.05]\%$ in weight, relative to water. For such concentration values, the PAAM solution can be considered in the dilute regime, where the polymer chains do not overlap. Previous works estimate the transition between dilute and semidilute regime, e.g., when the polymer chains overlap without entanglement, at $c \sim [0.06 - 0.1]\%$ [43,44]. This dilute regime was chosen for the relative low viscosity, similar to that of water, which allow to easily manipulate the magnetic particles.

We mix the hematite particle and the PAAM solution; the resulting suspension is then confined between a plastic petridish and a cover slip that are later sealed. The experimental cell, with a final thickness of $\sim$260 μm, is placed on the stage of a custom made optical microscope. The latter is connected to a charge-coupled device camera (Scout scA640-74f, Basler) that allows to record real-time videos of the particle dynamics at 75 frames per seconds. Videos of the growth process have been taken at a lower frame rate of 30 Hz. Further, the microscope is equipped with a set of custom-made magnetic coils having their axis aligned along the three orthogonal directions $(\hat{x}, \hat{y}, \hat{z})$. We generate a rotating magnetic field perpendicular to the substrate plane $(\hat{x}, \hat{z})$ by connecting four of the coils to a power amplifier (IMG STA-800, Stage Line) that was controlled via an arbitrary waveform generator (TGA1244, TTi).

III. REALIZATION OF PARALLEL ZIGZAG BANDS

Once dispersed in the polymer solution, the hematite particles sediment close to the bottom plane and display weak thermal fluctuations. To realize the colloidal shakers, we drive

these particles back and forward along a fixed direction (here the $\hat{x}$ axis) using a time dependent rotating field,

$$\boldsymbol{B} = B[\sin{(2\pi t \, \Delta f_-)}\hat{x} + \cos{(2\pi t \, \Delta f_+)}\hat{z}] \,. \quad (1)$$

Here B is the field amplitude, which we fix to $B = 5.5$ mT, f the driving frequency also fixed to $f = 80$ Hz, $\Delta f_{\pm} = f \pm \delta f/2$ and δf the frequency difference between the two fields components along the $\hat{x}$ and $\hat{z}$ axis, $\delta f = 4$ Hz. The field in Eq. (1) periodically changes the direction of rotation each $\delta t = 1/(2\delta f)$, and this effect has two consequences. First it aligns the permanent moments of the particles imposing a fixed orientation with respect to their long axis. Second, the particles are subjected to a magnetic torque $\boldsymbol{\tau}_m = \boldsymbol{m} \times \boldsymbol{B}$ which set them in rotational motion along their short axis at an angular speed $\Omega = 2\pi f$ and close to the bottom plane. Due to the rotational-translation hydrodynamic coupling [45], the spinning hematite performs periodic displacements back and forward following synchronously the field rotations. Indeed, we have independently checked that, for driving frequencies $f < 100$ Hz, the particles are in the synchronous regime, i.e., their magnetic moment is locked to the field by a constant phase-lag angle [46,47].

As shown in the sequence of images in Figs. 1(a) and 1(b), when the particles are homogeneously dispersed in a PAAM solution at a concentration $c_p = 0.05\%$, the applied modulation along the $\hat{x}$ direction induces the growth of large scale zigzag bands along the perpendicular, $\hat{y}$ direction. As time proceeds, the bands coarsen by acquiring neighboring particles and merge with nearest bands, forming one large structure that extends beyond the microscope observation area. Depending on the initial particle concentration, this structure can reach a length of a few mm and a thickness of $\sim$50μm, Fig. 1(b). Our protocol to create localized bands, such that the lateral growth (along $\hat{x}$) process can be entirely visualized, consists in transforming a large zigzag structure into a series of small clusters via application of an in-plane rotating magnetic field, $\boldsymbol{B} \equiv B[\cos{(2\pi ft)}\hat{x} - \sin{(2\pi ft)}\hat{y}]$, Fig. 1(c). As previously reported for different magnetic colloids in water [48,49] or nonmagnetic particles in a ferrofluid
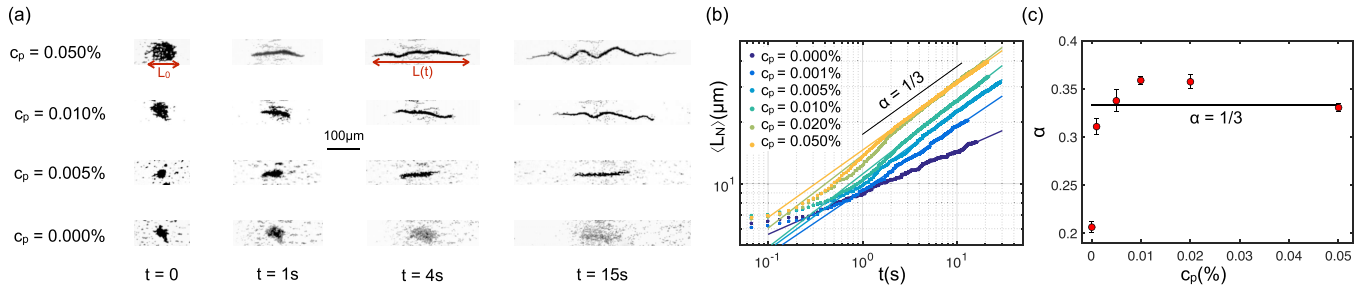
FIG. 2. (a) Table illustrating the evolution of clusters with initial length L_0 into bands of length $L(t)$ for different time t and concentration of dispersed polymer (PAAM) given by c_p. As shown in the first column, the used concentration $c_p \in [0, 0.05]\%$. The oscillating field [Eq. (1)] is applied at $t = 0$, and is the same for all PAAM concentrations. See corresponding video S2 in [39] for the case in pure water, showing the absence of zigzag structures. (b) Mean normalized length $\langle L_N \rangle = \langle L/N^{1/3} \rangle$ as a function of time t in log-log scale for different PAAM concentrations. Disks are experimental data, the solid lines are linear regressions used to extract the exponent α. (c) Exponent α as a function of the polymer concentration c_p.

[50], the rotating field applies a torque to each particle and also induces time-average dipolar attractions, which are not affected by the presence of the PAAM. Thus, the large band breaks into several rotating circular clusters composed of attractive spinning colloids. The size of these clusters result from the balance between the magnetic attraction and the repulsive hydrodynamic flow induced by the particle spinning motion [51]. After that, we apply again the oscillating field, Eq. (1), but now along the $\hat{y}$ direction, inducing the formation of parallel lines of shakers growing along the $\hat{x}$ axis, Fig. 1(d), see also video S1 in [39].

The table in Fig. 2(a) illustrates how the PAAM concentration affects the band growth at different times. For the largest amount of polymer tested ($c_p = 0.05\%$), we find that a circular cluster first collapses into a line in less than a second, then the line lengthens and becomes thinner since the number of particles is constant. After ~ 5 s, the line deforms and it acquires a zigzag shape where branches are arranged at a constant angle of $\theta_l = \pm 31°$. This effect was explained in Ref [38] by considering the shakerlike shape of the flow field generated by the particle rotation. Decreasing the PAAM concentration reduces the angle of the zigzag structures. While at high PAAM concentration the particles self-organize into zigzags with sharp tips that merge branches at a constant angle, at low PAAM concentration the stripes flatten, reducing this angle. Note that this effect occurs for all initial particles configurations, whether the particles are homogeneously distributed across the plane as shown in Fig. 1(a), or when they form localized clusters, as shown in Fig. 2(c). In pure water the cluster of oscillating particles does not form any band but rather grow uniformly due to diffusion, bottom row in Fig. 2(a), and also illustrated in video S2 in [39].

IV. BAND ELONGATION

To characterize the longitudinal growth of the clusters, we measure the length $L(t)$ as a function of time t for different polymer concentrations c_p. In Fig. 2(b) we divide L by $N^{1/3}$ with $\langle L_N \rangle = \langle L/N^{1/3} \rangle$ being N the number of particles within a cluster. We use this rescaling since the initial condition, i.e., the initial number of particles N, is difficult to control experimentally. To compute N, we measure the initial cluster diameter L_0, defining N and $N = (\pi (L_0/2)^2)/a_p$, a_p being the

area covered by a single particle. All curves shown in Fig. 2(b) display two distinct regimes: first $\langle L_N \rangle$ barely increases for times shorter than 1 s, which corresponds to the initial collapse of the cluster in a line. After that, the line grows as a power law with an exponent $\alpha = 1/3$ for all c_p except for pure water, where the dynamics are slower as governed by diffusion and possible weak hydrodynamic interactions, here $\alpha = 0.210 \pm 0.006$, Fig. 2(c). We note that, the exponent observed in our system is in general smaller than that measured when magnetic colloids form chains in water and under a static field, which was estimated to be $\alpha \geqslant 0.5$ [52]. This indicates a different growth mechanism which, in our case, is due to the presence of other interactions than magnetic dipolar ones.

To get more insight on the elongation behavior, we use particle tracking velocimetry to measure the flow field profile generated by the rotation of a single shaker as a function of c_p, Fig. 3(a), we provide more details in Appendix A. Without PAAM, the flow field is weakly attractive everywhere except at short distances, i.e., close to the particle tip where the streamlines converge to a stagnation point near the tip. Indeed, in a previous work [53] it was shown that close propelling hematite particles can create a hydrodynamic bound state where they align tip to tip, i.e., in agreement with the presence of this stagnation point. By adding PAAM the situation changes since elastic effects due to the polymer start to appear. In this situation, the flow profile becomes similar to that of a shakerlike force dipole [54], which is attractive at the particle side and repulsive along the two tips. It was shown previously, using a Oldroyd-B constitutive model [38], that this flow field is the consequence of the first normal stress induced by particles rotating in the viscoelastic fluid. By increasing the PAAM concentration, we observe that a vortex starts forming close to the particle tips ($\theta \approx 0$) and progressively moves to finally reach a position at $\theta \simeq 33°$. As shown in Fig. 3(b), an attractive and repulsive zone are separated by an angle $\theta_L \in [0, 33]°$ for $c_p \in [0, 0.05]\%$. As θ_L decreases, the zigzag flatten into a line, Fig. 2(a), $c_p = 0.005\%$, and it disappears for $c_p = 0\%$, Fig. 2(a), bottom row.

V. THEORY

We consider the zigzag band as a one dimensional (1D) chain of particles characterized by a spatial density $\rho(x, t)$
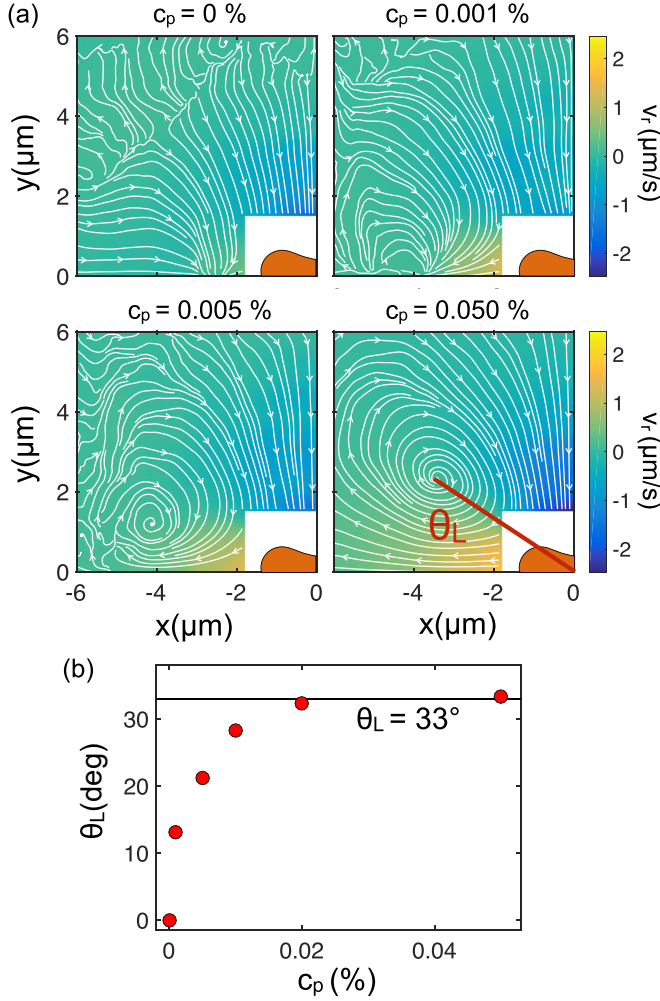
FIG. 3. (a) Panels showing the flow fields generated by a shaker for different PAAM concentrations. The color code shows the radial velocity v_r in the $(\hat{x}, \hat{y})$ plane of one shaker with the streamlines superimposed for four different PAAM concentration. Without PAAM, the flow field is mainly attractive and the fluid flows towards the colloidal shaker. As one raises c_p, a repulsive zone starts to appear leading to the formation, a vortex. The attractive and repulsive zones are separated by a line making an angle θ_L with the horizontal axis. (b) Limit angle θ_L as function of c_p.

and a local velocity $v(x, t)$. This velocity results from the hydrodynamic flow fields generated by all nearest particles. Moreover, since we reduce the problem to 1D, the interactions between the particles are purely repulsive ($\theta = 0$). Thus, the local velocity at position x is the integral of all the particles velocity:

$$v(x, t) = \int_D v_p(x - x')\rho(x', t)dx', \qquad (2)$$

$v_p(x - x')$ being the flow velocity that a particle at position x exerts on a particle at position x', and D is the domain of integration. Further, to simplify the problem, we assume that the flow velocity generated by a particle at a position x is equal to a constant v_p within the interval $[x - r_c \; ; \; x + r_c]$ and zero

elsewhere, with r_c being a cutoff length. Thus, we have

$$v(x, t) = v_p \int_{x - r_c}^{x + r_c} \text{sgn}(x - x')\rho(x', t)dx', \qquad (3)$$

being sgn the signum function. Since the zigzag band can be considered as isolated due to the relative large distance with nearest bands, as shown in Fig. 1(d), the total mass within a band is conserved

$$\frac{\partial \rho}{\partial t} = -\frac{\partial (v\rho)}{\partial x} \qquad (4)$$

and we search for a solution $(\rho(x, t), v(x, t))$ that satisfies both Eqs. (3) and (4). A solution of this problem is given by

$$\rho(x, t) = \frac{-x^2}{6v_p r_c^2 t} + \left(\frac{3N^2}{32 r_c v_p t}\right)^{1/3}$$

$$v(x, t) = \frac{x}{3t} \; ; \qquad (5)$$

more details are given in Appendix B. Since there are no particles outside the chain, the density $\rho(x, t)$ is zero at $x = \pm L/2$. Imposing this boundary condition, we arrive at

$$L(t) = \left(36 N v_p r_c^2 t\right)^{1/3}, \qquad (6)$$

and $L_N \propto t^{1/3}$. Equation (5) shows that the velocity scales linearly with space with a slope $1/3t$, and the density ρ is a parabola which becomes flat and wider with time.

To confirm these results, we have set up a minimal simulation scheme that reproduces the band growth using the velocity field from the experimental data. In particular, we obtained the relative velocity $\mathbf{v}_{\exp}(r_{ji}, \theta_{ji})$ between two particles as a function of their relative distance r_{ji} and angle θ_{ji}. These measurements were performed in a previous study [38]. Then, we fit the experimental data with an empirical function (see Appendix C for more details), and integrate the corresponding equation of motion:

$$\frac{d\mathbf{r}_i}{dt} = \sum_{j \neq i} \mathbf{v}(r_{ji}, \theta_{ji}) \qquad (7)$$

being $\mathbf{v}$ the velocity field around a particle. As an initial condition, we consider N particles randomly distributed within a ring of diameter $L_0 = 40 \, \mu\text{m}$ and at a packing fraction of $\phi = 0.7$, and we use as cutoff length $r_l = 20 \, \mu\text{m}$, beyond which the particles no longer interact, see Appendix C for more detail about the simulations. Note that when we set $r_l < L_0/2$, sometimes we observe in our simulations that the cluster collapses into two distinct bands which merge at a later stage. For $r_l \geqslant L_0/2$ instead, the cluster always collapses into a single band.

The simulations reproduce quantitatively the experimental results, as shown in Figs. 4(a) and 4(b). Indeed, the sequence of images in Fig. 4(a) display the behavior of an ensemble of shakers where the initial cluster collapses first into a line within ~1 second and later it lengthens with time similar to the experimental observations. For $c_p = 0.05\%$ the length L_N matches very well the experimental data showing the scaling $t^{1/3}$, as shown in Fig. 4(b). We further use the simulations to test the predictions of the model for $\rho(x, t)$ and $v(x, t)$. Indeed, compared to the experiments, the simulations allow to resolve all particle positions and speeds, a task that is difficult
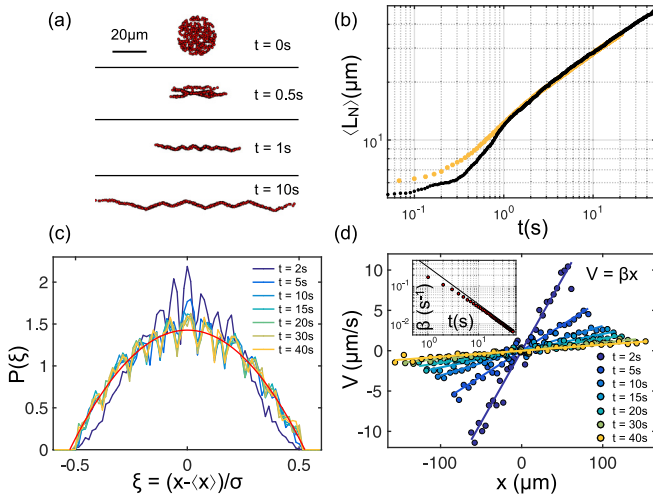
FIG. 4. Snapshots of a simulation at different times t. (b) Normalized mean length $\langle L_N \rangle$ as function of time, the experimental curve for $c_p = 0.05\%$ is in orange, the back curve is the results of the simulation. (c) Normalized distribution of particle $P(\xi)$ at different times t. The red curve is a parabolic fit of the curve at $t = 40\,\text{s}$. (d) Local velocity along the $\hat{x}$ axis as a function of x and at different times t. Points are results of the simulation, the solid lines are linear fit used to extract the slope β as a function of time. Inset: slope β as a function of time, dots are results of the simulation, the black line represents the function $y(t) = 1/3t$.

experimentally due to the large particle density. To confirm the predicted behavior of $\rho(x, t)$, we have computed the distribution of the normalized position $\xi = (x - \langle x \rangle)/\sigma$ at different times t, σ being the standard deviation of the particle positions. After a short transient regime, all distributions tend to collapse into a parabola, as predicted by the model, Fig. 4(c). Also, we observe that the local velocity $v(x, t)$ scales linearly with the position x displaying a slope equal to $1/3t$, as shown in the inset of Fig. 4(d).

VI. CONCLUSIONS

We have investigated the growth process of clusters made of shaking magnetic rollers which elongate into a zigzag structure within a viscoelastic medium. We observe that circular clusters first collapse into a line and later grow with time following a power law with an exponent $1/3$. The collapse find its origin in the attractive part of the flow field, Fig. 3, as revealed by particle tracking velocimetry. Thus, particles located at a relative angle $\theta > 33°$ attract each others and end up side by side while the interaction is repulsive for $\theta < 33°$. We simplify the problem by considering a one dimensional model and find that a constant repulsion between the shakers with a cutoff length is sufficient to explain the power-law growth and corresponding $1/3$ exponent. These predictions were tested numerically finding a good agreement. Moreover, the growth scenario remain similar by changing the added concentration of polymer, except for the case $c_p = 0\%$.

The possibility of controlling the linear growth of dense clusters of active particles may find different technological applications. For example, zigzag bands display a conveyor belt current along their edges able to drag nonmagnetic

particles. Such localized hydrodynamic flow could be used to transport chemicals or biological species along a desired location in a microfluidid chip. The use of rotating or translating magnetic inclusions to generate controlled flows within a microfluidic environment was demonstrated in previous works in Newtonian media [55–60]. We here show that these effects can be further extended to viscoelastic fluids, thus opening the doors toward direct applications in biological systems.

APPENDIX A: PARTICLE TRACKING VELOCIMETRY

We obtain the particle flow fields shown in the panels of Fig. 3(a) by performing particle tracking of passive, tracer spheres, dispersed with the peanut particles. The flow fields were obtained from a dilute solution of peanut particles, so that interactions between them are negligible, mixed with silica colloids of $1\,\mu\text{m}$ diameter that were used as tracers. We then record 26 videos of 1 min duration at 75 fps using an oil immersion $100\times$ Nikon objective. For these videos we tracked the position of both the peanut and the tracers. In particular, we considered a square region of $10\,\mu\text{m}$ around the peanut. This region was divided in square cells of lateral size $d = 0.05\,\mu\text{m}$. Inside these cells, the local mean relative velocities (velocity along $\hat{x}$ and $\hat{y}$ and radial $\hat{r}$ direction) between the peanut and the tracers are computed by averaging over all the particles inside the cell, over time and the different experimental videos). We then performed a spatial moving average with a square windows of size $21d = 1.05\,\mu\text{m}$. Since the flow field is symmetric, we further averaged the fourth quadrant of the image.

APPENDIX B: SOLUTION OF EQ. (4)

To find couples of solutions $(v(x, t), \rho(x, r))$ that satisfy both Eqs. (3) and (4), we numerically solve those two equations using as initial conditions

$$\rho(x, t = 0) = \frac{e^{-\frac{x^2}{2}}}{\sqrt{2\pi}}$$

$$v(x, t = 0) = v_p \int_{x-r_c}^{x+r_c} \text{sgn}(x - x') \frac{e^{-\frac{x'^2}{2}}}{\sqrt{2\pi}} dx'. \quad \text{(B1)}$$

In practice, we use a recursion method and calculate numerically the density $\rho(x, t + dt)$ using Eq. (3), and then $v(x, t + dt)$ from $\rho(x, t + dt)$ using Eq. (4). As nondimensional parameters, we use time step $dt = 0.1$, space step $dx = 0.01$, cutoff length $r_c = 1$, particle velocity $v_p = 0.1$,
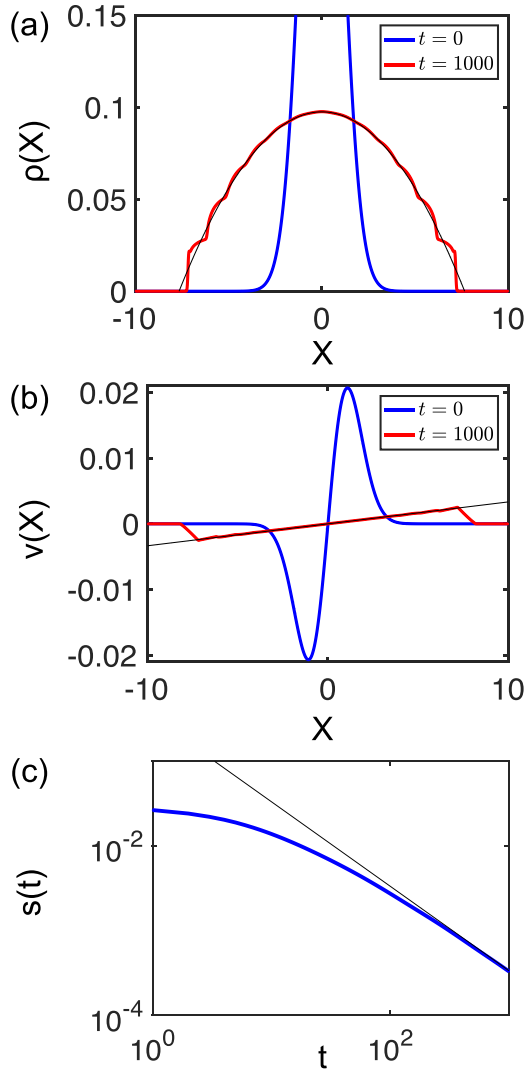
FIG. 5. Numerical resolution of Eqs. (3) and (4). (a) Density as a function of space at time $t = 0$ (blue) and $t = 1000$ (red). The black line is a fit of equation $y(x) = -ax^2 + b$ with $a = 0.00166$ and $b = 0.0974$. (b) Velocity as a function of space at time $t = 0$ (bue) and $t = 1000$ (red). The black line is a fit of equation $y(x) = cx$ with $c = 1/3000$. (c) Slope $s(t)$ of the velocity as function of time, $s(t)$ converges toward the line of equation $y(t) = 1/(3t)$ (black line).

and total space length $L_M = 100$. The numerical solutions $(v(x, t), \rho(x, t))$ have the form

$$v(x, t) = \frac{cx}{t},$$
$$\rho(x, t) = -x^2 f(t) + g(t), \qquad (B2)$$

with c a constant and $f(t)$, $g(t)$ arbitrary functions of time, and are shown in Fig. 5. Placing these solutions in Eq. (3) leads to

$$f(t) = \frac{a}{t^{3c}}, \quad g(t) = \frac{b}{t^c}, \qquad (B3)$$

with a and b constants. The density $\rho(x, t)$ then reads

$$\rho(x, t) = -\frac{ax^2}{t^{3c}} + \frac{b}{t^c}. \qquad (B4)$$

We further use the above expression of ρ in Eq. (4), which gives

$$v(x, t) = 2av_p r_c^2 \frac{x}{t^{3c}}. \qquad (B5)$$

As a result, we obtain the equation $2av_p r_c^2 \frac{x}{t^{3c}} = \frac{cx}{t}$, which implies

$$c = 1/3, \quad a = \frac{1}{6v_p r_c^2}. \qquad (B6)$$

To obtain the constant b we impose the following constraints, namely the integral of the density over L is equal to the total number of particles N, and the density is zero at $x = \pm L/2$,

$$N = \int_{-L/2}^{L/2} \rho(x, t) dx \quad \rho(\pm L/2, t) = 0, \qquad (B7)$$

which gives

$$N = \frac{-aL^3}{12t} + \frac{bL}{t^{1/3}}, \quad \frac{-aL^2}{4t^2} + \frac{b}{t^{1/3}} = 0. \qquad (B8)$$

Finally, one has

$$b = \left(\frac{3N^2}{32r_c^2 v_p}\right)^{1/3}, \quad L(t) = \left(36Nv_p r_c^2 t\right)^{1/3}, \qquad (B9)$$

and:

$$\rho(x, t) = \frac{-x^2}{6v_p r_c^2 t} + \left(\frac{3N^2}{32r_c v_p t}\right)^{1/3},$$
$$v(x, t) = \frac{x}{3t}. \qquad (B10)$$

APPENDIX C: NUMERICAL SIMULATION

In integrating Eq. (7), we consider two cases for the velocity $\boldsymbol{v}$, depending on a cut-off distance r_c. For $r_{ji} > r_c$, we assume that $\boldsymbol{v} = \boldsymbol{v}_{\exp}/2$ where $\boldsymbol{v}_{\exp}$ is an empirical function that describes the relative velocity between a pair of interacting particles measured experimentally at $c_p = 0.05\%$ [38]. Note that to have the velocity field $\boldsymbol{v}$, one has to divide $\boldsymbol{v}_{\exp}$ by two since $\boldsymbol{v}_{\exp}$ is the result of the contribution of two particles. Thus, $\boldsymbol{v}_{\exp}$ is given by

$$v_{\exp}(r_{ji}, \theta_{ji}) = (ar_{ji} + b)\exp\left(-r_{ij}^2/8\right) + c,$$
$$a = (\theta_{ji}/1.22)^{2/3}(3.12 + 4.4) - 3.12,$$
$$b = -(\theta_{ji}/1.22)^{2/3}(45 + 24) + 45,$$
$$c = -(\theta_{ji}/1.22)^{2/3}(0.3 + 0.4) + 0.3. \qquad (C1)$$

Since the interaction between two particles is essentially radial, we neglect the azimuthal contribution of the velocity and $\boldsymbol{v}_{\exp} = v_{\exp}\boldsymbol{e_r}$. At the end of a sequence of approach ($\theta_{ji} > \theta_l$), two particles come in close contact (side by side). In this situation, we observe that the pair exhibit a three-dimensional leap-frog dynamics [61], sliding on each other and ending tip to tip before repealing. To reduce the complexity of the simulation scheme, we did not consider this transitory leap-frog state, but rather take it into account as a "scattering" event. In simulations, two particles at a closer distance than r_c are placed at a relative position $r_{ji} = r_c$ and $\theta_{ji} = 0$ in one time

step:

$$v_x = \frac{r_c - \Delta x}{2dt}, \quad v_y = \frac{-\Delta y}{2dt}, \quad \text{(C2)}$$

with $\Delta x = x_i - x_j$, $\Delta y = y_i - y_j$. We perform numerical simulations of a system of N pointlike particles in a 2D square box of size L with periodic boundary conditions. We consider a second cut-off distance $r_l = 20$ μm beyond which the particles no longer interact, and $r_c = 0.2$μm. The particles follow the above mentioned dynamics, and we solve the equation of motion with an Euler scheme with a time step $dt = 10^{-2}$ s.

---

[1] T. Vicsek, A. Czirók, E. Ben-Jacob, I. Cohen, and O. Shochet, Novel type of phase transition in a system of self-driven particles, Phys. Rev. Lett. **75**, 1226 (1995).

[2] Y. Yang, V. Marceau, and G. Gompper, Swarm behavior of self-propelled rods and swimming flagella, Phys. Rev. E **82**, 031904 (2010).

[3] G. Wang, T. V. Phan, S. Li, M. Wombacher, J. Qu, Y. Peng, G. Chen, D. I. Goldman, S. A. Levin, R. H. Austin, L. Liu, Emergent field-driven robot swarm states, Phys. Rev. Lett. **126**, 108002 (2021).

[4] M. Y. B. Zion, Y. Caba, A. Modin, and P. M. Chaikin, Co-operation in a fluid swarm of fuel-free micro-swimmers, Nat. Commun. **13**, 184 (2022).

[5] F. Peruani, A. Deutsch, and M. Bär, Nonequilibrium clustering of self-propelled rods, Phys. Rev. E **74**, 030904(R) (2006).

[6] H. H. Wensink and H. Löwen, Aggregation of self-propelled colloidal rods near confining walls, Phys. Rev. E **78**, 031409 (2008).

[7] F. Peruani, T. Klauss, A. Deutsch, and A. Voss-Boehme, Traffic jams, gliders, and bands in the quest for collective motion of self-propelled particles, Phys. Rev. Lett. **106**, 128101 (2011).

[8] O. Pohl and H. Stark, Dynamic clustering and chemotactic collapse of self-phoretic active particles, Phys. Rev. Lett. **112**, 238303 (2014).

[9] F. Ginot, I. Theurkauff, D. Levis, C. Ybert, L. Bocquet, L. Berthier, and C. Cottin-Bizonne, Nonequilibrium equation of state in suspensions of active colloids, Phys. Rev. X **5**, 011004 (2015).

[10] Y. Shoham and N. Oppenheimer, Hamiltonian dynamics and structural states of two-dimensional active particles, Phys. Rev. Lett. **131**, 178301 (2023).

[11] J. Bialké, T. Speck, and H. Löwen, Crystallization in a dense suspension of self-propelled particles, Phys. Rev. Lett. **108**, 168301 (2012).

[12] C. A. Weber, C. Bock, and E. Frey, Defect-mediated phase transitions in active soft matter, Phys. Rev. Lett. **112**, 168301 (2014).

[13] A. Kudrolli, G. Lumay, D. Volfson, and L. S. Tsimring, Swarming and swirling in self-propelled polar granular rods, Phys. Rev. Lett. **100**, 058001 (2008).

[14] A. Kaiser, A. Snezhko, and I. S. Aranson, Flocking ferromagnetic colloids, Sci. Adv. **3**, e1601469 (2017).

[15] D. Nishiguchi, I. S. Aranson, A. Snezhko, and A. Sokolov, Engineering bacterial vortex lattice via direct laser lithography, Nat. Commun. **9**, 4486 (2018).

[16] G. S. Redner, M. F. Hagan, and A. Baskaran, Structure and dynamics of a phase-separating active colloidal fluid, Phys. Rev. Lett. **110**, 055701 (2013).

[17] I. Buttinoni, J. Bialké, F. Kümmel, H. Löwen, C. Bechinger, and T. Speck, Dynamical clustering and phase separation in suspensions of self-propelled colloidal particles, Phys. Rev. Lett. **110**, 238301 (2013).

[18] M. N. van der Linden, L. C. Alexander, D. G. A. L. Aarts, and O. Dauchot, Interrupted motility induced phase separation in aligning active colloids, Phys. Rev. Lett. **123**, 098001 (2019).

[19] F. Caballero and M. C. Marchetti, Activity-suppressed phase separation, Phys. Rev. Lett. **129**, 268002 (2022).

[20] R. Gross, M. Bonani, F. Mondada, and M. Dorigo, Autonomous self-assembly in swarm-bots, IEEE Trans. Robot. **22**, 1115 (2006).

[21] M. Rubenstein, A. Cornejo, and R. Nagpal, Programmable self-assembly in a thousand-robot swarm, Science **345**, 795 (2014).

[22] M. Z. Miskin, A. J. Cortese, K. Dorsey, E. P. Esposito, M. F. Reynolds, Q. Liu, M. Cao, D. A. Muller, P. L. McEuen, and I. Cohen, Electronically integrated, mass-manufactured, microscopic robots, Nature (London) **584**, 557 (2020).

[23] A. Snezhko and I. S. Aranson, Magnetic manipulation of self-assembled colloidal asters, Nat. Mater. **10**, 698 (2011).

[24] S. Sanchez, A. A. Solovev, S. M. Harazim, and O. G. Schmidt, Microbots swimming in the flowing streams of microfluidic channels, J. Am. Chem. Soc. **133**, 701 (2011).

[25] J. Simmchen, L. Baraban, and W. Wang, Beyond active colloids: From functional materials to microscale robotics, ChemNanoMat **8**, e202100504 (2022).

[26] H. C. Fu, T. R. Powers, and C. W. Wolgemuth, Theory of swimming filaments in viscoelastic media, Phys. Rev. Lett. **99**, 258101 (2007).

[27] E. Lauga, Propulsion in a viscoelastic fluid, Phy. Fluids **19**, 083104 (2007).

[28] J. Teran, L. Fauci, and M. Shelley, Viscoelastic fluid response can increase the speed and efficiency of a free swimmer, Phys. Rev. Lett. **104**, 038101 (2010).

[29] J. R. Gomez-Solano, A. Blokhuis, and C. Bechinger, Dynamics of self-propelled Janus particles in viscoelastic fluids, Phys. Rev. Lett. **116**, 138301 (2016).

[30] N. Narinder, C. Bechinger, and J. R. Gomez-Solano, Memory-induced transition from a persistent random walk to circular motion for achiral microswimmers, Phys. Rev. Lett. **121**, 078003 (2018).

[31] K. Qi, E. Westphal, G. Gompper, and R. G. Winkler, Enhanced rotational motion of spherical squirmer in polymer solutions, Phys. Rev. Lett. **124**, 068001 (2020).

[32] S. E. Spagnolie and P. T. Underhill, Swimming in complex fluids, Annu. Rev. Condens. Matter Phys. **14**, 381 (2023).

[33] C.-K. Tung, C. Lin, B. Harvey, A. G. Fiore, F. Ardon, M. Wu, and S. S. Suarez, Fluid viscoelasticity promotes collective swimming of sperm, Sci. Rep. **7**, 3152 (2017).

[34] H. C. Flemming and J. Wingender, The biofilm matrix, Nat. Rev. Microbiol. **8**, 623 (2010).

[35] A. Houry, M. Gohar, J. Deschamps, E. Tischenko, S. Aymerich, A. Gruss, and R. Briandet, Bacterial swimmers that infiltrate

and take over the biofilm matrix, Proc. Natl. Acad. Sci. USA **109**, 13088 (2012).

[36] J. L. Bigelow, D. B. Dunson, J. B. Stanford, R. Ecochard, C. Gnoth, and B. Colombo, Mucus observations in the fertile window: a better predictor of conception than timing of intercourse, Hum. Reprod. **19**, 889 (2004).

[37] T. Qiu, T.-C. Lee, A. G. Mark, K. I. Morozov, R. Münster, O. Mierka, S. Turek, A. M. Leshansky, and P. Fischer, Swimming by reciprocal motion at low Reynolds number, Nat. Commun. **5**, 5119 (2014).

[38] G. Junot, M. De Corato, and P. Tierno, Large scale zigzag pattern emerging from circulating active shakers, Phys. Rev. Lett. **131**, 068301 (2023).

[39] See Supplemental Material at http://link.aps.org/supplemental/ 10.1103/PhysRevResearch.6.013287 for two videos illustrating the dynamics of the magnetic shakers in the PAAM water solution.

[40] T. Sugimoto, M. M. Khan, and A. Muramatsu, Preparation of monodisperse peanut-type α-fe$_2$o$_3$ particles from condensed ferric hydroxide gel, Colloids Surf. A **70**, 167 (1993).

[41] F. Martinez-Pedrero, A. Cebers, and P. Tierno, Orientational dynamics of colloidal ribbons self-assembled from microscopic magnetic ellipsoids, Soft Matter **12**, 3688 (2016).

[42] F. Martinez-Pedrero, A. Cebers, and P. Tierno, Dipolar rings of microscopic ellipsoids: Magnetic manipulation and cell entrapment, Phys. Rev. Appl. **6**, 034002 (2016).

[43] A. Zell, S. Gier, S. Rafai, and C. Wagner, Is there a relation between the relaxation time measured in CaBER experiments and the first normal stress coefficient? J. Non-Newton. Fluid. Mech. **165**, 1265 (2010).

[44] F. D. Giudice, G. D'Avino, F. Greco, I. D. Santo, P. Netti, and P. L. Maffettone, Particle alignment in a viscoelastic liquid flowing in a square-shaped microchannel, Lab Chip **13**, 4263 (2013).

[45] J. Happel and H. Brenner, *Low Reynolds Number Hydrodynamics* (Noordhoff, Leyden, The Netherlands, 1973).

[46] P. Tierno, J. Claret, F. Sagués, and A. Cēbers, Overdamped dynamics of paramagnetic ellipsoids in a precessing magnetic field, Phys. Rev. E **79**, 021501 (2009).

[47] G. Junot, A. Cebers, and P. Tierno, Collective hydrodynamic transport of magnetic microrollers, Soft Matter **17**, 8605 (2021).

[48] P. Tierno, R. Muruganathan, and T. M. Fischer, Viscoelasticity of dynamically self-assembled paramagnetic colloidal clusters, Phys. Rev. Lett. **98**, 028301 (2007).

[49] N. Osterman, I. Poberaj, J. Dobnikar, D. Frenkel, P. Ziherl, and D. Babić, Field-induced self-assembly of suspended colloidal membranes, Phys. Rev. Lett. **103**, 228301 (2009).

[50] P. Pieranski, S. Clausen, G. Helgesen, and A. T. Skjeltorp, Braids plaited by magnetic holes, Phys. Rev. Lett. **77**, 1620 (1996).

[51] H. Massana-Cid, D. Levis, R. J. H. Hernández, I. Pagonabarraga, and P. Tierno, Arrested phase separation in chiral fluids of colloidal spinners, Phys. Rev. Res. **3**, L042021 (2021).

[52] J. Faraudo, J. S. Andreu, C. Calero, and J. Camacho, Predicting the self-assembly of superparamagnetic colloids under magnetic fields, Adv. Funct. Mater. **26**, 3837 (2016).

[53] F. Martinez-Pedrero, A. Ortiz-Ambriz, I. Pagonabarraga, and P. Tierno, Emergent hydrodynamic bound states between magnetically powered micropropellers, Sci. Adv. **4**, eaap9379 (2018).

[54] Y. Hatwalne, S. Ramaswamy, M. Rao, and R. A. Simha, Rheology of active-particle suspensions, Phys. Rev. Lett. **92**, 118101 (2004).

[55] A. Terray, J. Oakey, and D. W. M. Marr, Microfluidic control using colloidal devices, Science **296**, 1841 (2002).

[56] T. Sawetzki, S. Rahmouni, C. Bechinger, and D. W. M. Marr, In situ assembly of linked geometrically coupled microdevices, Proc. Natl. Acad. Sci. USA **105**, 20141 (2008).

[57] P. Tierno, R. Golestanian, I. Pagonabarraga, and F. Sagués, Magnetically actuated colloidal microswimmers, J. Phys. Chem. B **112**, 16525 (2008).

[58] B. Kavčič, D. Babič, N. Osterman, B. Podobnik, and I. Poberaj, Magnetically actuated microrotors with individual pumping speed and direction control, Appl. Phys. Lett. **95**, 023504 (2009).

[59] I. Kavre, G. Kostevc, S. Kralj, A. Vilfand, and D. Babič, Fabrication of magneto-responsive microgears based on magnetic nanoparticle embedded pdms, RSC Adv. **4**, 38316 (2014).

[60] F. Martinez-Pedrero and P. Tierno, Magnetic propulsion of self-assembled colloidal carpets: Efficient cargo transport via a conveyor-belt effect, Phys. Rev. Appl. **3**, 051003(R) (2015).

[61] H. Massana-Cid, E. Navarro-Argemí, D. Levis, I. Pagonabarraga, and P. Tierno, Leap-frog transport of magnetically driven anisotropic colloidal rotors, J. Chem. Phys. **150**, 164901 (2019).